Hypersonic Inflatable Aerodynamic Decelerator Earth-based Applications

Soumyo Dutta*
NASA Langley Research Center, Hampton, VA, 23681, USA

Evan Roelke†, Alejandro Pensado‡, and Michael Manwell†
Analytical Mechanics Associates, Hampton, VA, 23681, USA

Hypersonic Inflatable Aerodynamic Decelerators technology has been developed by NASA to enable challenging entry, descent, and landing missions at various planetary destinations. In the last two decades, HIAD technology has been developed through a series of ground tests and flight tests, culminating in the 2022 Low-Earth Orbit Flight Test of an Inflatable Decelerator flight demonstration of a 6 m diameter vehicle from orbital velocities. Past studies have considered application of HIAD for human-scale missions, especially return from the Moon or human-class missions to Mars. However, recent commercial interest in the HIAD technology following LOFTID's success shows HIAD applications are possible for cislunar return, Earth aerocapture, return from low Earth orbit, and even launch vehicle component recovery. This paper describes the flight performance range for these new, Earth-based applications.

I. Introduction

Hypersonic Inflatable Aerodynamic Decelerator (HIAD) technology has been in development at NASA for the last two decades and has expanded the boundary for the use of deployable aeroshells. For many entry, descent, and landing (EDL) applications, maximum heating and deceleration loads can be decreased with low aeroshell ballistic coefficient (β), which is a ratio of the system mass (m) to the drag coefficient (C_D) and aerodynamic reference area (S_{ref}) that is in turn defined by the aeroshell diameter. For high mass missions, such as human-scale missions to Mars, a low β is most readily attained through increases in the aeroshell diameter. However the fairing diameter of launch vehicles, typically around 4 m, limits the diameter of the aeroshell. Deployable aeroshells, such as HIAD, can be stowed within the confines of the launch vehicle fairing diameter during launch, and can expand to a larger diameter upon separation from the launch vehicle.

$$\beta = \frac{m}{C_D * S_{ref}} \tag{1}$$

Several ground and flight tests of the HIAD have matured the technology for potential cislunar return and Mars landing human-class missions. Four flight tests, including Inflatable Reentry Vehicle Experiment (IRVE) in 2007 [1], IRVE-II in 2009 [2, 3], IRVE-3 in 2011 [4, 5], and Low-Earth Orbit Flight Test of an Inflatable Decelerator (LOFTID) in 2022 [6–8], have pushed the development of the HIAD article, culminating in the 6 m diameter LOFTID aeroshell.

Past work has considered the application of HIAD to human-scale missions, such as Earth-return from the Moon [4] or Mars EDL [9, 10]. Furthermore, the HIAD system can also be utilized for non-human scale missions as well, such as the emerging commercial space sector at Earth. This paper looks at the potential use of HIAD for various Earth EDL applications, including return from cislunar space, aerocapture into Earth orbit, payload recovery from low Earth orbit, and return of boosters of launch vehicles. This paper briefly examines recent HIAD development and describes the current modeling and simulation being conducted to generate the results for new HIAD applications. Additionally, the references cited in this paper provide a literature review of the HIAD technology. The readers can delve into these papers for in-depth analysis of several HIAD-related topics that are not covered in this paper.

*Aerospace Engineer, Atmospheric Flight and Entry Systems Branch, MS 489, AIAA Associate Fellow.
†Aerospace Engineer, Atmospheric Flight and Entry Systems Branch, MS 489, AIAA Member.
‡Aerospace Engineer, Atmospheric Flight and Entry Systems Branch, MS 489, AIAA Senior Member.

II. HIAD Applications

A. Recent HIAD Development

HIAD technology has had three successful flight tests in the last 15 years that demonstrate the viability of the technology to a large array of applications. Figure 1 shows a schematic comparison of the recent HIAD flight test articles and Table 1 summarizes some of the key parameters of the test. The first IRVE flight test is omitted here as there was not experiment due an anomoly with the launch vehicle for the HIAD. The no test still helped with HIAD development as the test article was made and improved the HIAD manufacturing process. IRVE-II was a built-to-print replica of the original IRVE article [3].

As seen in Table 1, the entry velocity has increased with each mission, making the peak heat flux higher as well. For HIAD, the thermal protection system (TPS) is flexible, and this flexible TPS (FTPS) can either be a generation 1 (Gen-1) material, such as Nextel that is designed for heat flux up to 30 W/cm^2, or a Gen-2 material, such as Silicon Carbide (SiC) which has been designed for heat flux up to 50 W/cm^2 [11]. The IRVE flights used Gen-1 FTPS [11, 12], while LOFTID was tested with Gen-2 [13] with an eye towards Mars applications that will have higher heat flux requirements.

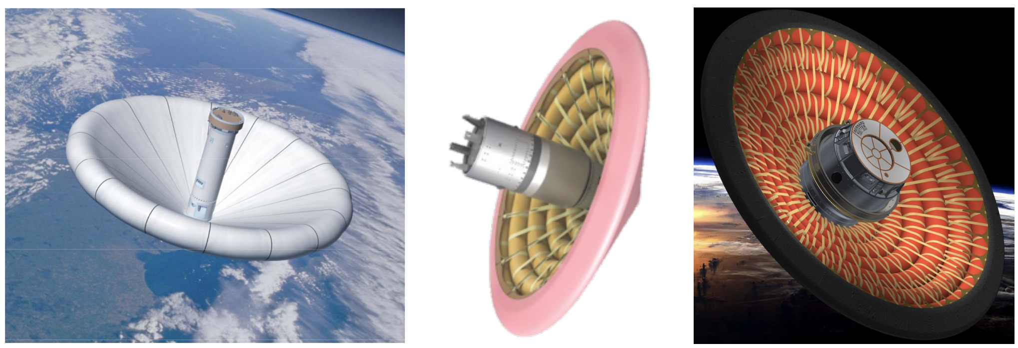

(a) 2009 IRVE-II (b) 2012 IRVE-3 (c) 2022 LOFTID

Fig. 1 Past Successful HIAD Flight Tests.

Table 1 Details of the Recent HIAD Flight Tests.

Parameters	IRVE-II [3, 14, 15]	IRVE-3 [5]	LOFTID [7, 8, 13]
Year of Test	2009	2012	2022
Diameter (m)	2.93	3.0	6.0
Nose Radius (m)	0.387	0.191	1.71
Sphere-cone Angle (deg)	60	60	70
Entry Mass (kg)	124.6	281	1100
Ballistic Coefficient (kg/m^2)	13.6	29.2	24.7
Planet-Relative Entry Velocity (km/s)	1.6	2.7	8.0
Peak Heat Flux (W/cm^2)	2.2	15.0	39.8
Thermal Protection System	Gen-1	Gen-1	Gen-2

B. Past HIAD Applications Considered

The work in Ref. [4] looked at extending the application of HIAD to various types of missions after the success of the IRVE-II and IRVE-3 missions. That paper focused on the high-mass, human-scale missions, such as high energy return from the Moon and Mars on-board the Multi-Purpose Crew Vehicle (MPCV) or several Mars entry missions, aerocapture, fast transit, and direct-entry to high altitudes. These cases are summarized in Table. 2 from Ref. [4]. Most of these applications are at multiple metric tons (t) entry mass, some require large HIADs in excess of 15 m diameter, and some of the concepts also require a non-zero lift-to-drag (L/D) ratios. As a point of comparison, the past HIAD flight tests were 3-6 m in diameter, and ranged from 0.1-1.1 t in mass.

Table 2 Summary of high-mass HIAD applications from Ref [4].

Scenario	Details	Entry Velocity (km/s)	Entry Mass (t)	HIAD Diameter (m)	Ballistic Coefficient (kg/m^2)
Launch Asset Recovery	2nd Stage Recovery	7.7	4	5	140
Launch Asset Recovery	1st Stage Recovery	3.5	22	10	200
Mars Aerocapture	Aerocapture 500 km circular orbit, L/D=0.2	7.4	10.5	9	141
Mars Aerocapture	Aerocapture 500 km circular orbit, L/D=0.2	9.5	14	26	23
Mars Southern Highlands	HIAD to supersonic/subsonic retro-propulsion	5.8	4	10	37.8
Mars Southern Highlands	HIAD to subsonic retro-propulsion	5.8	4	15	17
Hybrid Lunar Return	Hybrid Lunar return, direct entry	11	10.8	18	33
Mars Fast Transit	400 km circular orbit capture at Earth, L/D=0.2	12	7	21	17.5
Mars Fast Transit	400 km circular orbit capture at Earth, L/D=0.2	12	14	27	20
L2 to Low-Earth orbit Transfer	Hybrid L2 to Low-Earth orbit aerocapture, L/D=0.2	11.5	11.5	23	24

C. New Applications

The aim of this paper is slightly different from the Ref. [4] and more focused on commercial applications around Earth, such as cislunar return for smaller scale vehicles, aerocapture around Earth orbit, payload recovery from low Earth orbit, and sub-orbital recovery of booster stages of launch vehicles. These applications can be large, ranging up to 20 t in mass, but the HIAD diameters, with a few exceptions, are mostly in the range of what was used for the flight tests previously mentioned.

The applications considered for this paper are broken up into three areas:

1) Aerocapture and Orbit Change
2) Low Earth Orbit (LEO) Return
3) Suborbital Flight

Within the aerocapture area, two different scenarios – a simple orbit change and another that has aerocapture followed by EDL – are considered. Two different LEO return scenarios are also studied to show the differences between small mass return (0.35 t, 3 m diameter concept) or a larger mass return (6 t, 10 m diameter concept). Section IV has the detailed results looking at the trade space from these scenarios.

However, to get a holistic comparison between the past HIAD flights and the new scenarios, the trajectory spaces are compared in Fig. 2. The altitude, velocity, load, and heat flux trade space of completed HIAD missions and planned applications are shown. The HIAD flight tests had entry speeds below 8 km/s, and the newer commercial applications are also in the same range, with the exception of the first pass of aerocapture after lunar return. Compared to the human-scale missions discussed in Ref. [4], the altitude-velocity space are similar to already HIAD demonstrated capabilities. The story is similar for peak loads (noted here in terms of kilopounds or kips). The LOFTID trajectory is close to the range for most missions. The big exception is the suborbital return of launch vehicle stages. This mission has a peak load several times larger than the LOFTID limit. Finally, as the peak heat fluxes for the HIAD flight tests are summarized in Table 1, the Sutton-Graves convective, cold-wall indicator-based heat fluxes for the newer HIAD applications are shown. The rationale behind using his indicator are explained in Sec. III.B.3 and the user should note that the margined, total heat flux for these applications are on the order 20-50% higher than shown in these plots, but the trends for various scenarios are still clear.

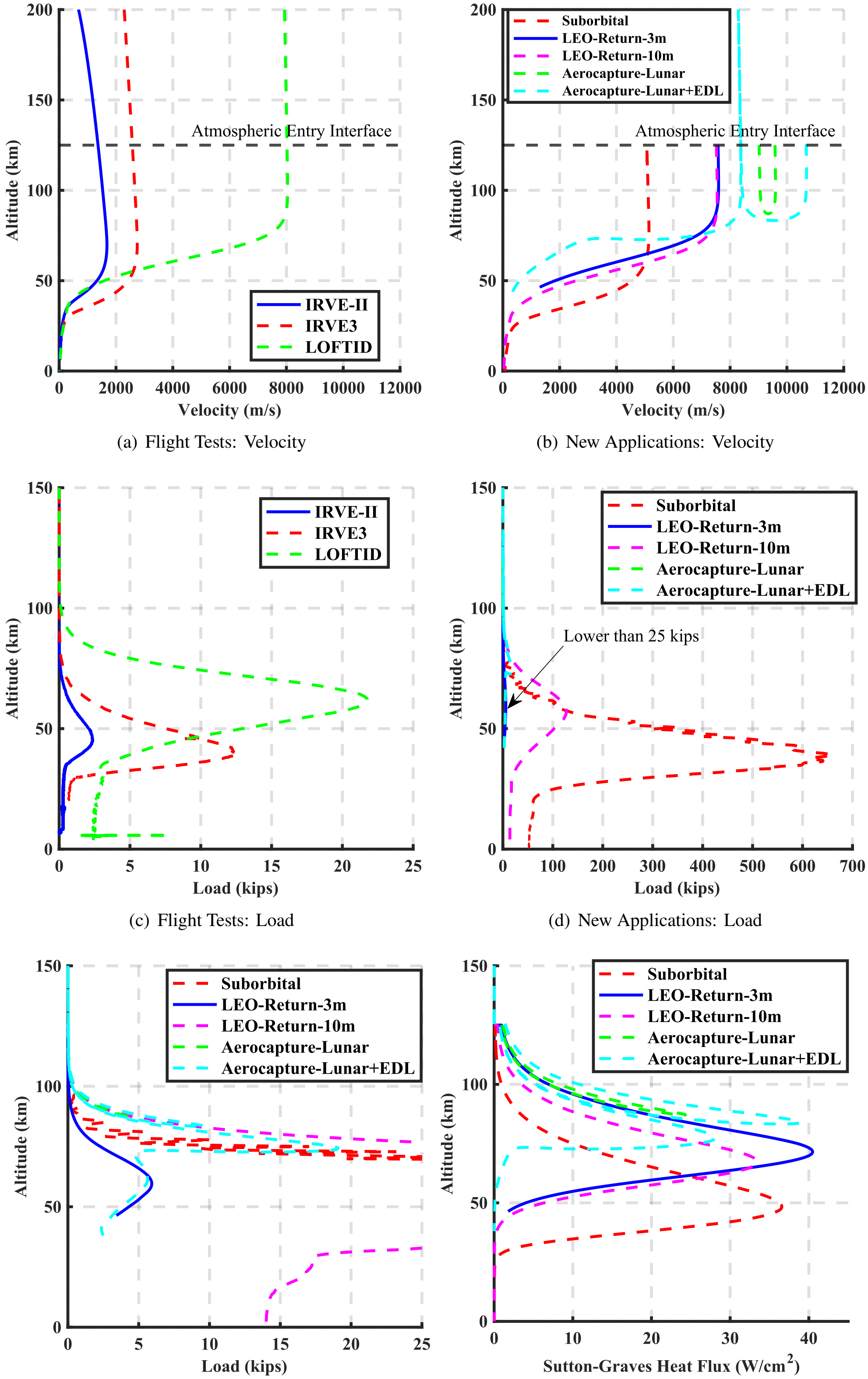

(a) Flight Tests: Velocity

(b) New Applications: Velocity

(c) Flight Tests: Load

(d) New Applications: Load

(e) New Applications (zoomed-in): Load

(f) New Applications: Heat Flux

Fig. 2 Comparison of flight conditions for past HIAD flights and future HIAD applications.

III. Modeling and Simulation

The Program to Optimize Simulated Trajectories II (POST2) [16] is the tool used for the EDL simulations covered for the various scenarios in this paper utilizing the HIAD technology. POST2 is a six degree-of-freedom (DOF) flight dynamics simulation tool and is a generalized point mass, discrete-parameter targeting and optimization trajectory simulation program with multi-vehicle capabilities that integrates translational and rotational equations of motion along the trajectory. The simulation tool has significant EDL flight heritage as it has been used in the past successfully for several Mars EDL missions, such as Mars Pathfinder [17], Mars Exploration Rovers [18], Mars Phoenix [19], Mars Science Laboratory [20], Mars InSight [21], and Mars 2020 [22]. Recently, many Earth EDL missions have leveraged this tool for their EDL operations, including Stardust [23], Genesis [24], ASPIRE [25], ADEPT [26], and OSIRIS REx [27]. More importantly for HIAD applications, POST2 has been used for modeling IRVE-II [3], IRVE-3 [5], and LOFTID [7].

A. Assumptions

Although the scenarios studied in this paper range from aerocapture from high energy entries to suborbital flights, the modeling and simulation has common assumptions and models. The common models, such as aerodynamics and atmosphere, are discussed in Sec. III.B, while the common assumptions are discussed here.

The shared ground rules and assumptions for the scenarios in this paper are:

- All analysis presented are for 3 DOF analysis. Thus, only translational equations of motion were analyzed, while the attitude is constrained, whether to 0 degree angle of attack or a specific trim value for a desired L/D.
- In similar vein to before, no active Guidance, Navigation, and Control (GNC) is performed in any of the scenario.
- POST2 models vehicles as rigid body vehicles at the center of mass. Flexible dynamics that might be demonstrated in deployables are not modeled explicitly in the simulations or are captured in the uncertainties of the aerodynamics models that are covered in Sec. III.B.2. That said, the previous HIAD flights have also had the rigid body assumption for their flight mechanics simulations and the results from flight reconstruction have agreed well with the predictions from the rigid body simulations. Thus, the rigid body assumption, even for deployables like HIAD, for the most part seems to be a good assumption to predict flight mechanics performance.
- The HIAD is a deployable decelerator that has a finite inflation time after separation during exoatmospheric flight [28]. For all of the scenarios considered here, the HIAD is assumed to be inflated. For the suborbital return flights, there might be timeline pressure for inflation, but that fidelity has not been captured in the results here.
- Most of the EDL scenarios as well as past HIAD flights have utilized a recovery parachute for the terminal phase of the flight, after the flight experiment or the key objectives have been met. However, the designs of the recovery parachute system are varied and since the focus of this paper is HIAD performance, the parachute modeling was ignored. Key HIAD performance parameters, such as peak heat flux, deceleration, etc., that are presented in this paper are for a stage of flight well before any parachutes would be required.
- The initial conditions for these scenarios are all provided by mission designers outside the HIAD team. These conditions are often parameterized for trade space analysis, but are also based on the very specific requirements analyzed in these scenarios. Future applications of the HIAD to similar scenarios may have different initial conditions, but the trends covered in the paper would be useful for mission designers during planning.

Additional assumptions for specific scenarios are discussed in Sec. IV.

B. Models

This section summarizes some engineering models used by the different simulations developed to cover various HIAD scenarios. The HIAD simulations have leveraged the work done by simulations for the previous successful HIAD flight tests [5, 7], and hence have utilized proven models when possible. These methods in guidance, aerodynamics, aerothermodynamic indicators, and atmospheric models are discussed in this section.

1. Entry Guidance

While previous HIAD flight tests flew in a ballistic configuration (zero angle of attack), future applications might desire to fly at a non-zero angle of attack whilst employing an active guidance algorithm such as bank angle modulation or direct force control in order to target an entry termination phase or aerocapture exit state [9, 10]. The former method involves invoking a change in the vehicle bank angle to rotate its lift force vector out of plane for range control, while direct force control involves directly modulating aerodynamic angles, namely angle of attack and angle of side slip. Both of these methods have been investigated for both aerocapture and direct entry cases with bank angle modulation having significant flight heritage, notably being employed on missions including Mars Science Laboratory (MSL) [29, 30] and Mars 2020 [31].

During entry guidance, the vehicle's control authority will nominally bound its trajectory by the constant lift-up and lift-down profiles, respectively. These bounding trajectories affect resultant constraining variables such as peak heat flux and peak acceleration. Therefore, guidance and steering enables the vehicle to mitigate constraints such as peak heat rate and peak sensed deceleration while simultaneously targeting a desired state. Because HIADs enable larger vehicle diameters (and thus lower ballistic coefficients), the spacecrafts are generally afforded lower peak heat fluxes at the expense of higher peak sensed deceleration during flight. However, modern guidance algorithms such as the Fully Numerical Predictor for Entry Guidance (FNPEG) can solve for guidance commands that meet such constraint limitations [32]. While this paper does not consider any trajectories with active guidance, it does explore the tradespace involving constant lift-up or lift-down as it relates to constraining variables such as heating and vehicle loads.

2. Aerodynamics

The aerodynamic models used for the simulations for the scenarios covered in this paper have been developed for various iterations of the HIAD project. For the orbital return missions, the LOFTID aerodatabase developed for a 70 deg. sphere-cone was used. This database, described in Ref. [33], is based on computational fluid dynamics (CFD) analysis, covering rarefied non-continuum flight all the way to subsonic continuum regime, as well as some ballistic range test data for dynamic aerodynamic coefficients. For the non-70 deg. sphere-cone aerodynamics, an aerodatabase built for the proposed High-Energy Atmospheric Reentry Test (HEART) [34] was used. This aerodatabase is primarily based on Newtonian aerodynamics for the hypersonic continuum regime and also contained some subsonic wind tunnel data. The aerodatabase provided data for various sphere-cone angles and has previously been used for HIAD-based studies in Refs. [9, 10]. For some suborbital return trajectories, especially those for 65 deg. sphere cone, the aerodatabase developed for the Vulcan Engine Return Aeroshell experiment as part of the Vulcan engine reuse project was used. This mission is discussed in Ref. [35]. This aerodatabse is based on primarily CFD analysis run at conditions potentially experienced during the suborbital return.

3. Aeroheating

Aeroheating indicators are generally developed for specific flight conditions and may not be extensible to various different scenarios. For example, the LOFTID mission developed aerothermal indicators, discussed in Ref. [36], that were proven to be reliable based on flight reconstruction, but these indicators are very specific for the LOFTID-like flight trajectory. Similarly, the HIAD Mission Applications study [4] from the early 2010's also developed some heating indicators that were very specific to the conditions studied in that project. Additionally, these very specific heating indicators are often not published openly in literature.

The purpose of this paper was to provide examples of HIAD performance that would be easily accessible to the readers and easier to test where HIAD applications could be useful. Hence, the aeroheating results provided in this paper rely on the Sutton-Graves convective, stagnation point heating indicator for air [37], which is widely known and available. Eq. 2 shows that for this indicator, heat flux (q) is a function of a constant (C_{SG}), freestream density (ρ_∞), nose radius (r_n), and freestream velocity (V_∞). However, Sutton-Graves is for convective, stagnation point heating with a cold-wall assumption. The qualifications that have to be attached to this indicator shows the limitation of these numbers, since important heating considerations such as radiative heating, turbulence, roughness augmentation, or margin policy have not been taken into account. Thus, the heating values in this paper should be looked at for trends rather than the specific heating value.

$$q = C_{SG} * \sqrt{\rho_\infty * r_n} * V_\infty^3 \tag{2}$$

4. Atmosphere

All of the applications covered in this study were at Earth, and hence the Earth Global Reference Atmospheric Model (Earth GRAM) was used for the analysis. Some of the scenarios used the Earth GRAM 2010 version of the model [38], while others used the updated Earth GRAM that is part of the GRAM Suite [39]. The updated GRAM Suite has incorporated more recent atmospheric data, but the results presented in this paper are not highly sensitive to these updated atmospheric conditions. In general, the atmospheric models provided dispersed atmospheric parameters, such as density, pressure, temperature, winds, and speed of sound, and these models were integrated into the flight dynamics simulation such that with change in location or time during the integration of the flight trajectory, the GRAM models were called to provide updated freestream conditions.

IV. Results

A. Aerocapture

Spacecraft returning to Earth may desire to capture into orbit or prior to a direct entry, such as a skip-entry trajectory employed during the Apollo missions [40]. One viable method of capturing into orbit is to use a maneuver called aerocapture, which involves flying through the upper atmosphere of a planetary body to dissipate orbital energy, resulting in an enclosed orbit upon atmospheric exit [41]. The same independent variables for direct entry are of interest for aerocapture applications, including entry flight path angle, entry velocity, ballistic coefficient, and L/D (which is a useful surrogate for control authority). This section will present the broad trade space results for aerocapture trajectories leveraging constant lift-to-drag ratios, with planet-relative entry velocities ranging from 10-12 km/s and planet-relative entry flight-path angles (EFPAs) between -6 and -4 degrees. Figure 3 depicts the tradespace results of several variables as functions of the vehicle's ballistic coefficient and EFPA. Note, the dissipated ΔV in Fig. 3(d) captures the decrease in velocity and energy from the initial trajectory an aerocapture pass through the atmosphere can accomplish, not the ΔV needed after aerocapture, which is usually a very small value when active guidance is employed.

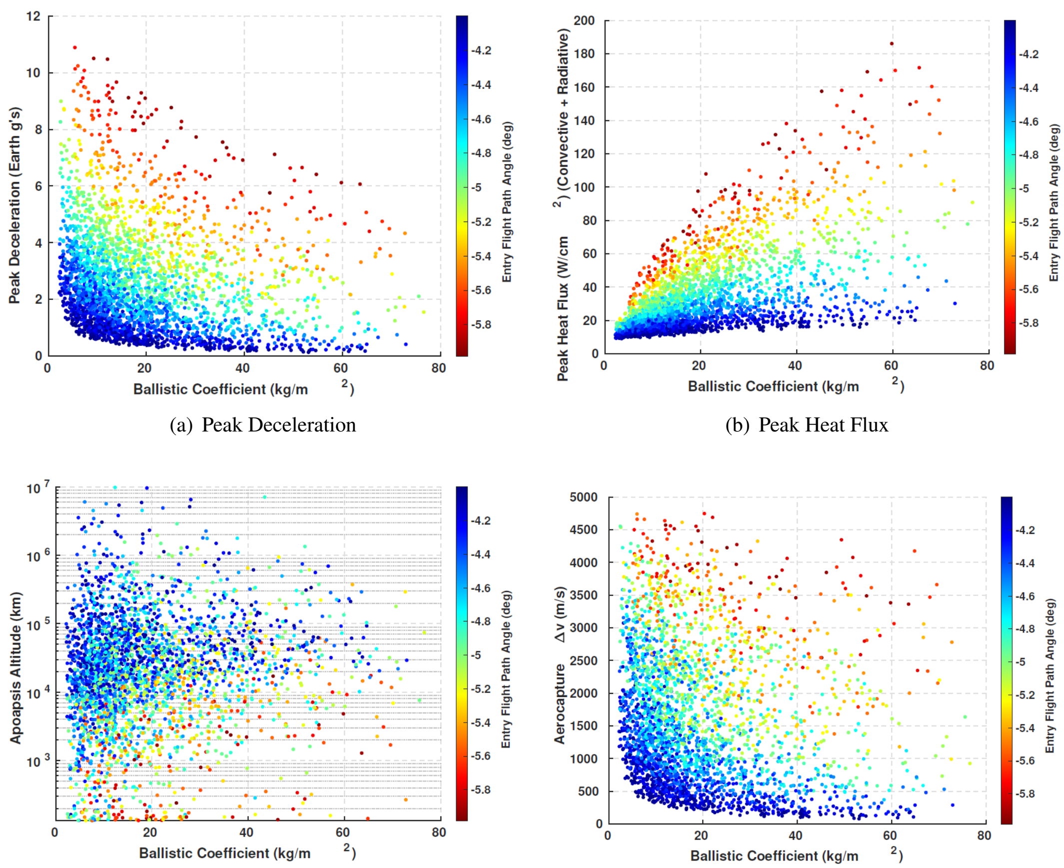

(a) Peak Deceleration (b) Peak Heat Flux

(c) Apoapsis Altitude (d) Dissipated ΔV

Fig. 3 HIAD Aerocapture trade space as function of ballistic coefficient

Primary variables of consideration for aerocapture applications are post-aerocapture orbit apoapsis and the amount of ΔV consumed by the aerocapture maneuver in addition to typical EDL tradespace parameters of interest including peak heat flux and peak sensed acceleration. Note that the scarcity of steep EFPA data points is because the given vehicle properties and initial conditions prevented the vehicle from exiting the atmosphere, resulting in a failed aerocapture maneuver. One potential solution could be active guidance that would modulate between lift up and lift down commands, but that was not explored as part of this work. Trades on HIAD diameter, cone angle, and vehicle mass are combined as figures considering the ballistic coefficient. The nose radius is assumed to be 25% of the HIAD diameter for these generalized trade space results. The vehicle's ballistic coefficient is generally increased through larger mass vehicle and/or smaller HIAD diameters, so Figure 3 can also be interpreted as functions of these parameters by holding the other constant. For example, increasing the payload mass will increase the ballistic coefficient, driving both peak deceleration and peak heat flux up.

The bottom row of plots show the post-aerocapture apoapsis altitude and the ΔV reduction from the maneuver itself. These parameters are shown to be heavily dependent on the vehicle's ballistic coefficient. A lower ballistic coefficient vehicle will dissipate more energy within the atmosphere (assuming all other variables constant) compared to a higher ballistic coefficient. This higher energy loss corresponds to a lower post-aerocapture orbital apoapsis. Additionally, steeper EFPAs are shown to result in lower apoapsis altitudes and higher ΔV reductions because the vehicle dives deeper into the atmosphere where atmospheric density, and therefore the drag force, are greater.

Figure 4 shows the results of the same dependent variables but as a function of L/D and EFPA. A negative L/D corresponds to a vehicle that has its lift vector pointed down throughout the trajectory (180 deg bank), while a positive L/D maintains a vertical lift vector during flight (0 deg bank). Note that direct force control actuators would most likely be limited to L/D ratios of ±0.1, while bank angle modulation mechanism design could offer L/D up to the demonstrated ±0.2 range shown. Vehicles with constant lift-down could dissipate more than the required amount of energy, leading to a reduced ability to exit the atmosphere and thus leaving gaps in the post-aerocapture apoapsis altitudes (Fig. 4(c)). The higher apoapsis altitude trajectories dissipate less energy within the atmosphere due to either lower EFPAs or higher ballistic coefficients, resulting in lower overall peak deceleration and peak heat flux values.

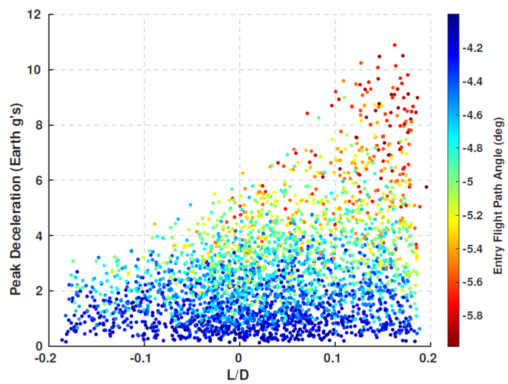

(a) Peak Deceleration

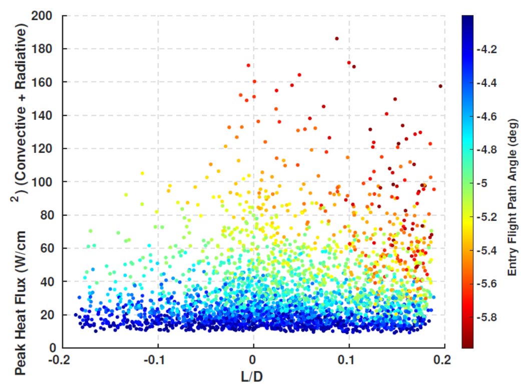

(b) Peak Heat Flux

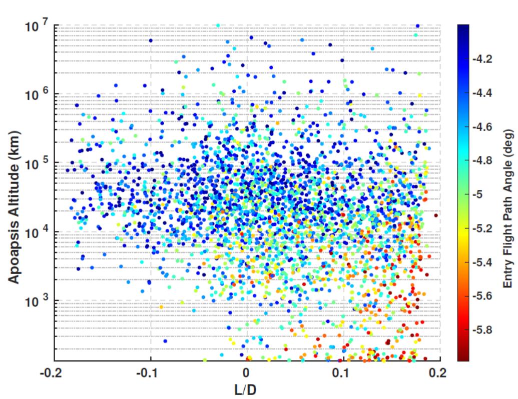

(c) Apoapsis Altitude

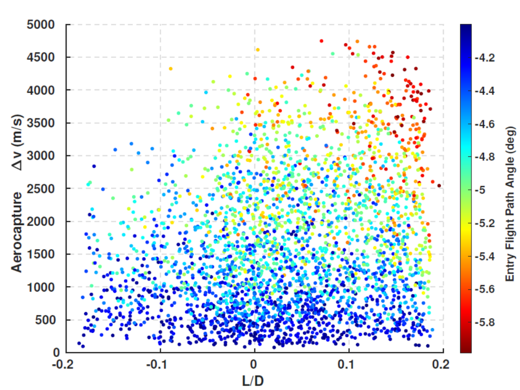

(d) Aerocapture ΔV

Fig. 4 HIAD Aerocapture trade space for constant-lift vehicle

Aerocapture is a lucrative applications for HIADs due to the lower peak heat flux and peak deceleration environments compared to a direct entry. But considerations of the thermal protection systems must be taken into account if the maneuver is followed up by a direct entry trajectory. One potential risk is the TPS material turning into glass after being heated initially if the vehicle operates exo-atmospherically too long post-aerocapture. Additionally, the TPS has to be certified to be capable of tolerating the dual heat pulse of aerocapture and then direct entry.

B. Reentry from Low Earth Orbit

For LEO mission applications, the design space can be bifurcated based on small or large payloads.

1. Small HIAD

Re-entry from Low Earth orbit is lucrative application for HIADs. For example, Ref. [42] has looked at the system implications of design a HIAD for small scale vehicles, like SmallSats. The trade space for designing a HIAD is driven by the entry conditions such as the planet relative velocity, EFPA, the ballistic coefficient, the cone angle, the nose radius, and the L/D of the vehicle, similar to what was seen in the aerocapture application. However, for small payload return from LEO, of the range of 100-500 kg, the size of the HIAD is small, and for this study HIAD diameters within 2.5 - 3.5 meters using a 70 deg cone angle were evaluated. The deorbit maneuver was considered as fixed, and therefore the planet relative velocity was treated as a fixed value for all cases at entry interface. The three key metrics to evaluate the feasibility of the design are the peak deceleration loads, the peak heat flux, and the total heat load. These define requirements for the toroids and thermal protection system design of the HIAD. Fig 5 shows the trade space in terms of the EFPA, ballistic coefficient, and L/D. For these sensitivities the cone angle of the vehicle is fixed to 70 deg and the nose radius is 0.5 m (to keep the central payload volume constant). For peak deceleration the trade space is the most sensitive to the entry flight path angle and the lift-to-drag ratio. Similarly, Fig. 6 shows the sensitivity of the peak heat flux with respect to the EFPA, ballistic coefficient, and lift-to-drag ratio. The heat flux shows a stronger correlation with ballistic coefficient and EFPA, with higher values at higher ballistic coefficients and steeper EFPA. The L/D correlation is as strong.

Relative to previous flight tests as discussed in II.C, the deceleration for the smaller HIADs are smaller and the peak heat flux is consistent with other studies. The trade space can be further refined by evaluating the impact of the HIAD geometry such as the diameter and the nose radius as this defines the constraints of the payload. Table 3 shows the impact of of increasing the nose radius and the diameter for a non-lifting trajectory. Increasing the nose radius reduces the peak the flux, which is expected due to the inverse scaling nose radius has on heat flux using Sutton-Graves model (see Eq. 2). Increasing the diameter also reduces the peat heat flux but only has a small increase in the peak deceleration. However, increasing both diameter and nose radius would reduce geometric constraints of the payload. Table 4 illustrates the effects of increasing mass and diameter for a HIAD with a nose radius of 1.5 meters. The peak deceleration decreases slightly as mass increases or diameter increases, as ballistic coefficient (see Eq. 1) is not strongly correlated with deceleration. Conversely, the peak heat flux rises with an increase in mass and drops with an increase in diameter. These trade studies aim to characterize the design space for a smaller HIAD, although further analysis is needed to fully develop a HIAD design for a specific scenario of return from LEO.

Table 3 Nose Radius Trade Study for LEO Return using Small HIAD

Nose Radius (m)	Diameter (m)	Peak Deceleration (Earth g's)	Peak Heat Flux (W/cm^2)	Total Heat Load (kJ/cm^2)
0.75	2.50	7.79	41.39	4.51
	2.75	7.87	37.79	4.08
	3.00	7.95	34.79	3.72
	3.25	8.01	32.23	3.42
	3.50	8.07	30.00	3.16
1.00	2.50	7.79	35.84	3.91
	2.75	7.87	32.73	3.53
	3.00	7.95	30.12	3.22
	3.25	8.01	27.91	2.96
	3.50	8.07	25.98	2.74

Table 4 Mass and Diameter Trade Study for LEO Return using Small HIAD

Mass (kg)	Diameter (m)	Peak Deceleration (Earth g's)	Peak Heat Flux (W/cm^2)	Total Heat Load (kJ/cm^2)
150	2.50	7.99	23.46	2.55
	2.75	8.07	21.41	2.30
	3.00	8.14	19.65	2.10
	3.25	8.23	18.16	1.93
	3.50	8.30	16.88	1.78
200	2.50	7.87	26.93	2.97
	2.75	7.95	24.59	2.69
	3.00	8.02	22.63	2.45
	3.25	8.09	20.94	2.25
	3.50	8.15	19.46	2.08
300	2.50	7.70	32.67	3.69
	2.75	7.78	29.85	3.34
	3.00	7.85	27.48	3.04
	3.25	7.91	25.46	2.79
	3.50	7.98	23.72	2.58

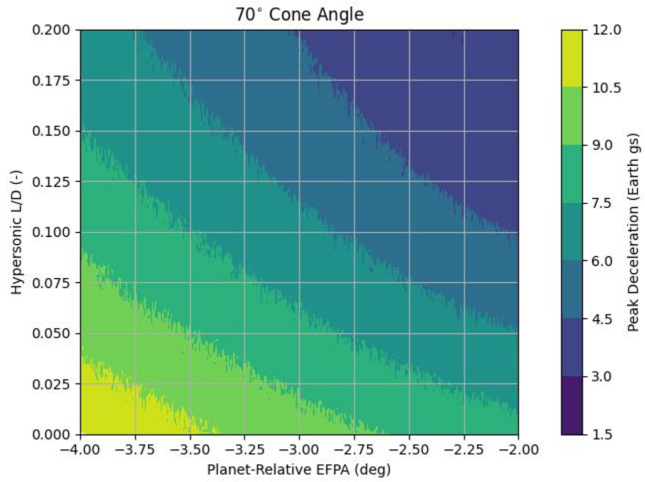

(a) Flight Path Angle vs. Lift-to-Drag Ratio

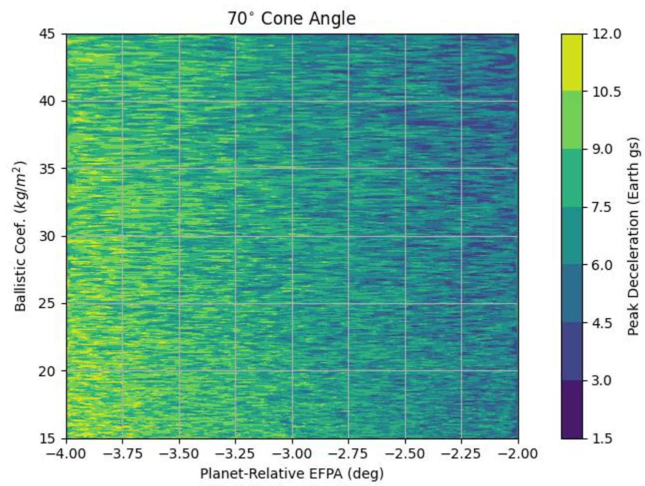

(b) Flight Path Angle vs. Ballistic Coefficient

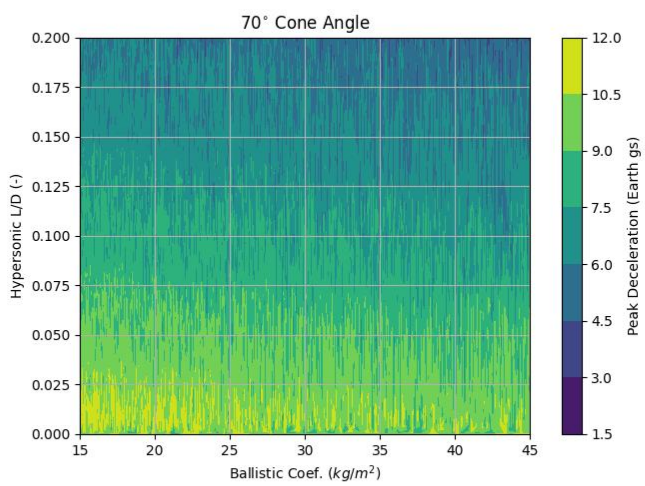

(c) Ballistic Coefficient vs. Lift-to-Drag Ratio

Fig. 5 Trade space for small HIAD application: Peak deceleration.

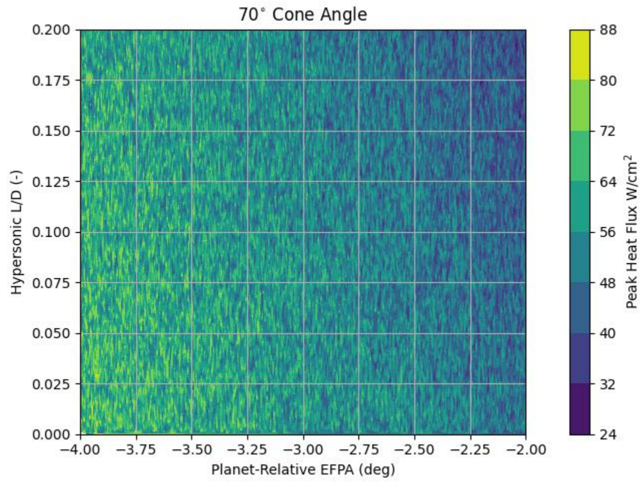

(a) Flight Path Angle vs. Lift-to-Drag Ratio

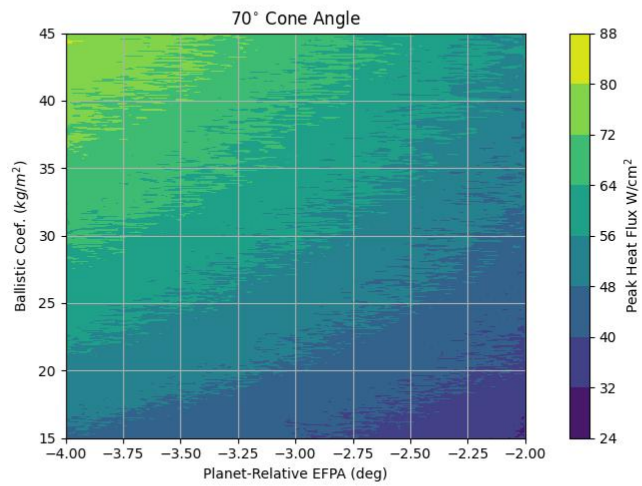

(b) Flight Path Angle vs. Ballistic Coefficient

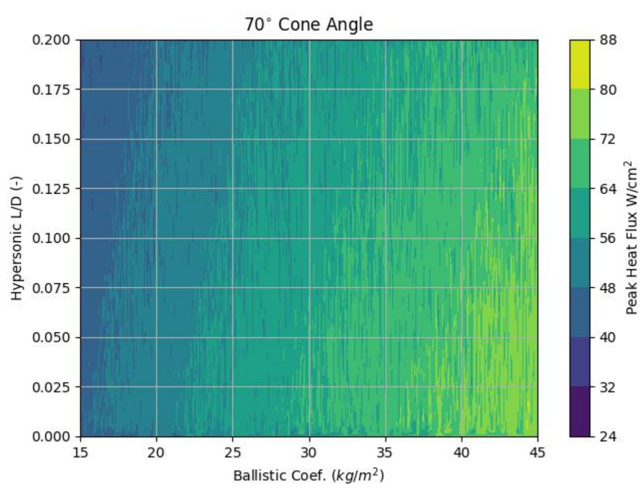

(c) Ballistic Coefficient vs. Lift-to-Drag Ratio

Fig. 6 Trade space for small HIAD application: Max Heat Flux.

2. Large HIAD

Another LEO return scenario considered include the return of higher mass (> 1 t) payloads in a ballistic (L/D = 0) trajectory, such as modules returning from the International Space Station. Although these modules are magnitudes larger than the types of payloads discussed in the previous subsection, they have designs that are driven by similar entry conditions such as EFPA and planet relative velocity. For this larger payload return from LEO, this study evaluated HIAD diameters of 9 and 10 meters using a 70 deg sphere cone design, fixed mass of ~7t, and nose cone radius of 33% of the HIAD diameter.

The deorbit maneuvers could vary in burn lengths, resulting in unique entry conditions summarized in Table 5. The nominal deorbit burn occurs around low Earth orbit altitudes and lasts for approximately 160 s. As the time of deorbit increases from 0 to 200 s, the entry velocity slightly decreases as the flight path angle becomes steeper. Table 6 shows the results of the effects of the deorbit burn on critical metrics of interest. As the deorbit burn increases, the peak deceleration and peak heat flux increase as a result of the steeper flight path angle at entry interface. Inversely, the total heat load decreases as the deorbit burn increases as a result of the steeper flight path angle producing a shorter total time of flight. The peak deceleration slightly increases by going from a 9 m to a 10 m HIAD design, while conversely cause the heating metrics to decrease.

Table 5 Deorbit Burn Affect on Entry Conditions: Large HIAD

Length of Deorbit Burn (s)	Relative Entry Velocity (km/s)	Relative Entry Flight Path Angle (deg)
0	7.58	-1.92
30	7.57	-2.08
60	7.56	-2.32
90	7.55	-2.54
120	7.53	-2.73
160	7.52	-2.96
200	7.50	-3.17

Table 6 Deorbit Burn Trade Study: Large HIAD

Diameter (m)	Deorbit Burn Length (s)	Peak Deceleration (g's)	Peak Heat Flux (W/cm^2)	Heat Load (kJ/cm^2)
9	0	7.31	27.76	3.32
	30	7.51	28.78	3.20
	60	7.85	30.24	3.03
	90	8.2	31.47	2.90
	120	8.55	32.51	2.80
	160	8.99	33.66	2.69
	200	9.41	34.56	2.60
10	0	7.38	23.91	2.82
	30	7.59	24.80	2.71
	60	7.95	26.05	2.57
	90	8.32	27.10	2.46
	120	8.69	27.98	2.37
	160	9.14	28.95	2.28
	200	9.56	29.73	2.20

C. High Ballistic Coefficient/Booster Recovery

One of the areas of commercial interest for the HIAD is to use the deployable to recover launch vehicle stages, specifically second stage or the engines (see Ref. [35]). These missions will be suborbital in nature, as the second stage of a launch vehicle would not have attained enough energy to get into a low Earth orbit. However, due to the mass of the engines as well as constraints such as low deceleration and heat flux required to allow the engines to be reused, the design of the HAID recovery system can be challenging. This scenario was briefly studied by the prior HIAD applications paper [4], but the HIAD design after the success of the LOFTID system allows for additional flexibility in the trade space.

Several different second stage recovery scenarios are considered here, include low energy scenarios such as low Earth orbit (LEO) launch vehicles with low or mid-energy trajectories, geosynchronous Earth orbit (GEO) launch vehicles with high-energy trajectories, and geosynchronous transfer orbit (GTO) launch vehicles with mid or high-energy trajectories. The launch vehicle trajectories in the paper have been generalized as much as been possible to not be reliant on any proprietary material, but applications for individual launch vehicle may vary due to the capability of that system.

Figure 7 shows the trade space in terms of ballistic coefficient and lift-to-drag ratio for peak deceleration. The range of ballistic coefficient are much higher than those of the previous HIAD flight tests (see Table 1), and hence these situations are considered as high ballistic coefficient applications in this paper. The plot shows the maximum sensed acceleration conditions for many different ballistic coefficient and lift-to-drag ratios. There is no clear trend in ballistic coefficient, which means going to larger diameters (lower ballistic coefficient vehicles) would not necessarily reduce loading, but there is a clear trend in decreasing peak sensed acceleration for higher, lift-up ratios. Thus, a moderately lifting system (L/D $\approx$ 0.1) could have a sizeable impact on peak deceleration.

However, the largest decrease in sensed acceleration in Fig 7 can be seen between the original series of trajectories and the decremented trajectories. Decremented trajectories have had an additional thrust maneuver after booster separation to reduce the vehicle energy and target a shallower flight path angle [35]. If the booster has additional capacity to do such an extra maneuver, the recovery system design could accommodate a lower deceleration-rated system, but often the additional decrement comes at the cost of added capability of the launch vehicle's to-orbit mass.

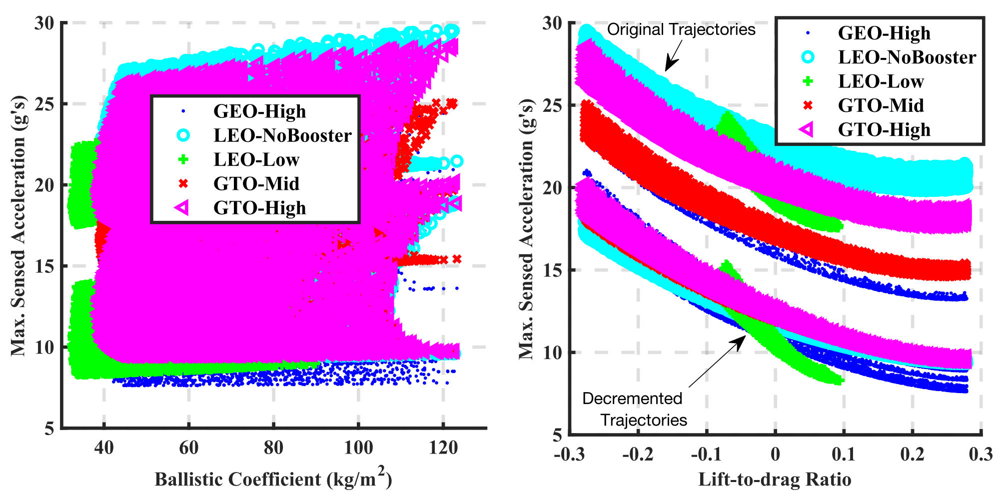

(a) Ballistic Coefficient (b) Lift-to-drag Ratio

Fig. 7 Trade space for the suborbital booster return scenario with HIAD: Peak deceleration.

The peak heat flux with Sutton-Graves heating indicator (Fig. 8) and total integrated heat load (Fig. 9) are also provided as a function of ballistic coefficient and lift-to-drag ratio. Recall from Sec. III.B.3 that the specific heat flux values in this paper are not high fidelity, as they are missing radiative heating, turbulence effects, and other parameters. But going to larger HIAD diameters (lower ballistic coefficient) has a sizeable effect on heat flux, which might allow the vehicles to use Gen-1 TPS from IRVE-II and IRVE-3 rather than the more capable but more expensive Gen-2 TPS from LOFTID. The integrated heat load is typically used for TPS sizing, the process for which is not covered in this paper. The reader is referred to Ref. [43] for more information.

An additional trade besides ballistic coefficient and lift-to-drag ratio is in the realm of the sphere-cone angle of

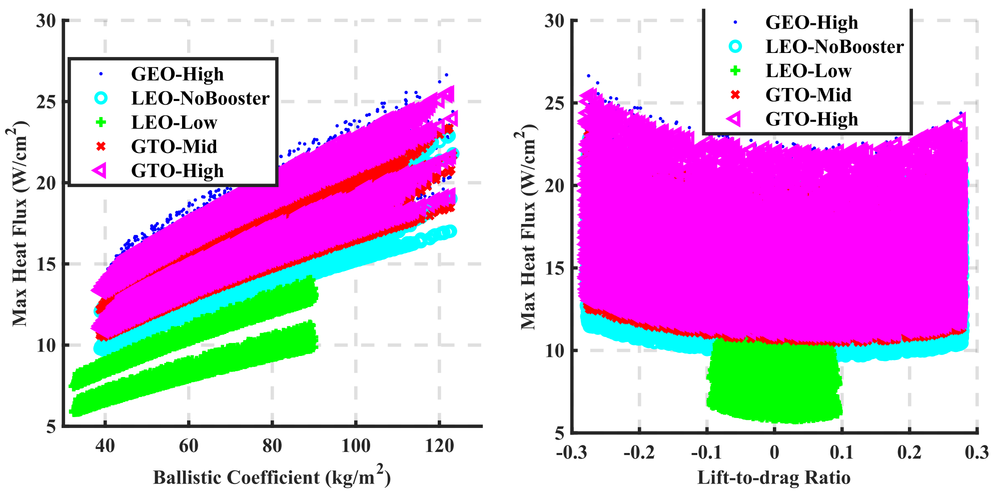

(a) Ballistic Coefficient (b) Lift-to-drag Ratio

Fig. 8 Trade space for the suborbital booster return scenario with HIAD: Peak heat flux with Sutton-Graves heating indicator.

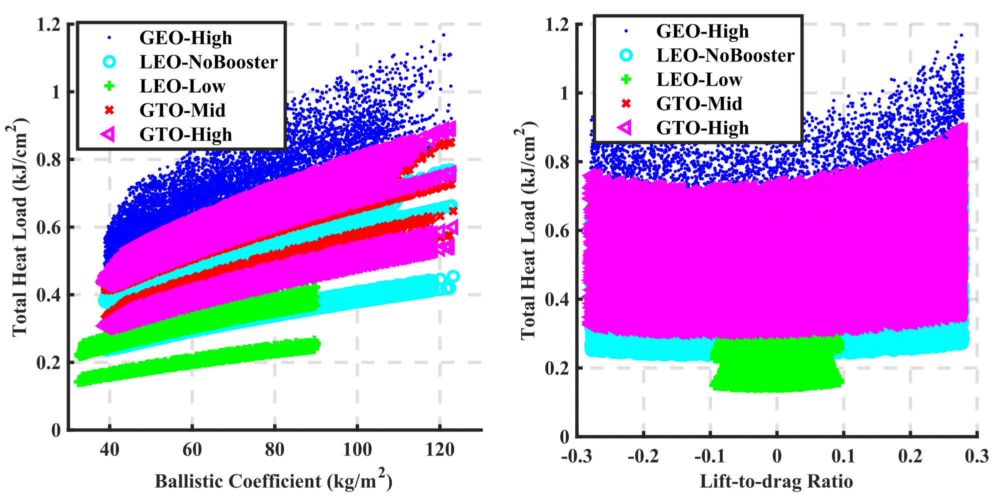

(a) Ballistic Coefficient (b) Lift-to-drag Ratio

Fig. 9 Trade space for the suborbital booster return scenario with HIAD: Total heat load.

the HIAD. LOFTID was a 70 deg. sphere-cone while the two successful IRVE missions were 60 deg. sphere-cone (Table 1). For Earth EDL applications, previous missions have tended to be 60 deg. sphere-cone [27, 44, 45] while Mars applications have required 70 deg. sphere-cone [17] primarily because the Earth atmosphere is denser than the Martian atmosphere and hence does not require higher drag-area from a more blunter body like a 70 deg. sphere-cone. That said, when the range of HIAD diameters are held constant, the 70 deg. sphere-cone vehicle does produce lower ballistic coefficient solutions that lead to lower peak deceleration (Fig. 10) and lower peak heat flux (Fig. 11). Additionally, a 70 deg. sphere-cone vehicle produces a slightly larger range of lift-to-drag ratio at a given angle of attack than a 60 deg. sphere-cone vehicle, which in turn leads to lower peak loads and heat flux. Thus, a trade in sphere-cone angles will be also beneficial for a specific HIAD design in the booster recovery application.

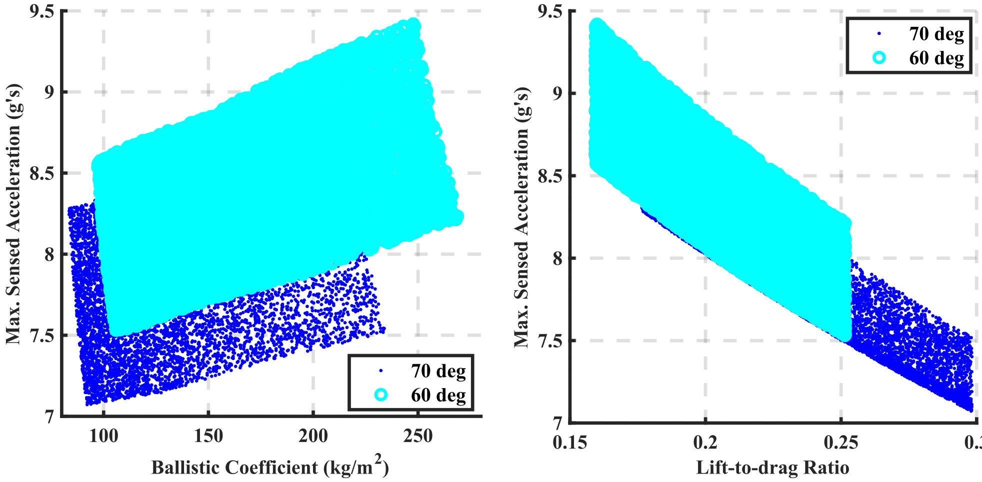

(a) Ballistic Coefficient

(b) Lift-to-drag Ratio

Fig. 10 Sphere-cone angle trade space for the suborbital booster return scenario with HIAD: Peak deceleration.

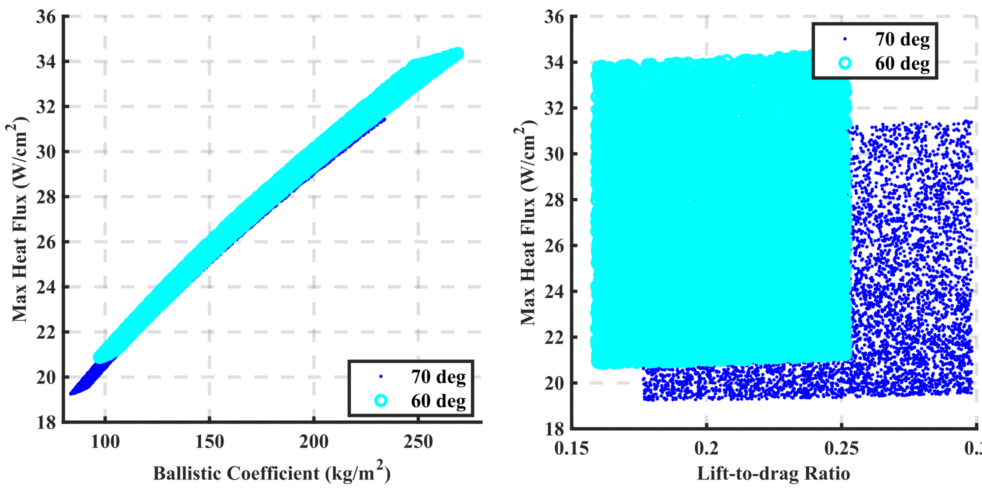

(a) Ballistic Coefficient

(b) Lift-to-drag Ratio

Fig. 11 Sphere-cone angle trade space for the suborbital booster return scenario with HIAD: Peak heat flux with Sutton-Graves heating indicator.

V. Conclusions

The HIAD technology has progressed significantly over the last two decades through a series of ground and flight tests. The 2022 LOFTID flight experiment demonstrated a successful EDL from orbital speeds for the largest blunt-body aeroshell ever flown. In the past, the HIAD technology has been shown to be useful for heavy-mass missions, like human-scale Earth return from the Moon or landing on Mars. But recent advent in commercial applications near Earth has raised several Earth-based applications for the HIAD, such as payload return from cislunar space, orbital maneuvering at Earth using aerocapture, low Earth orbit return to the Earth surface, or recovery of booster stages from launch vehicles. This paper shows the design space for such commercial missions with HIAD as the key technology. Future mission designers could contemplate the applicability of HIAD for their applications from the performance tabulated in this paper for various scenarios.

Acknowledgments

The authors acknowledge the help of the HIAD project at NASA Langley Research Center. Special thanks goes to F. Neil Cheatwood, the Principal Investigator of the HIAD project, and John DiNonno, the HIAD portfolio Chief Engineer, for their review of the work presented in this paper, and to Ashley Korzun, Brian Hollis, and Hisham Shehata, who have developed many of the aerodynamic models used in this study.

References

[1] Hughes, S., Dillman, R., Starr, B., Stephan, R., Lindell, M., Player, C., and Cheatwood, F., "Inflatable Re-entry Vehicle Experiment (IRVE) Design Overview," AIAA 2005-1636*, AIAA Aerodynamic Decelerator Systems (ADS) Conference,* Munich, Germany, 2005. https://doi.org/10.2514/6.2005-1636.

[2] Hughes, S., Cheatwood, F., Dillman, R., Wright, H., DelCorso, J., and Calomino, A., "The Hypersonic Inflatable Aerodynamic Decelerator (HIAD) Mission Applications Study," AIAA 2011-2524*, AIAA Aerodynamic Decelerator Systems (ADS) Conference,* Dublin, Ireland, 2011. https://doi.org/10.2514/6.2011-2524.

[3] O'Keefe, S., and Bose, D., "IRVE-II Post-Flight Trajectory Reconstruction," AIAA 2010-7515, *AIAA Atmospheric Flight Mechanics Conference,* Toronto, Canada, 2010. https://doi.org/10.2514/6.2010-7515.

[4] Bose, D., Winski, R., Shidner, J., Zumwalt, C., Johnston, C., Komar, D., Cheatwood, F., and Hughes, S., "The Hypersonic Inflatable Aerodynamic Decelerator (HIAD) Mission Applications Study," AIAA 2013-1389*, AIAA Aerodynamic Decelerator Systems (ADS) Conference,* Daytona Beach, FL, 2013. https://doi.org/10.2514/6.2013-1389.

[5] Olds, A. D., Beck, R. E., Bose, D. M., White, J. P., Edquist, K. T., Hollis, B. R., Lindell, M. C., Cheatwood, F. M., Gsell, V. T., , and Bowden, E. L., "IRVE-3 Post-Flight Reconstruction," AIAA 2013-1390*, AIAA Aerodynamic Decelerator Systems Conference,* Daytona Beach, FL, 2013. https://doi.org/10.2514/6.2013-1390.

[6] DiNonno, J., and Cheatwood, F., "Low-Earth Orbit Flight Test of an Inflatable Decelerator (LOFTID) Mission Overview and Science Return," AIAA 2024-1309*, AIAA SciTech 2024,* Orlando, FL, 2024. https://doi.org/10.2514/6.2024-1309.

[7] Deshmukh, R., Dutta, S., Bowes, A., and DiNonno, J., "Flight Mechanics Analysis of Low-Earth Orbit Flight Test of an Inflatable Decelerator," AIAA-2024-1501, *AIAA SciTech 2024 Forum,* Orlando, Florida, 2024.

[8] Karlgaard, C., Deshmukh, R., Dutta, S., Korzun, A., and Hollis, B., "Trajectory Reconstruction of the Low-Earth Orbit Flight Test of an Inflatable Decelerator," AIAA-2024-1502, *AIAA SciTech 2024 Forum,* Orlando, Florida, 2024.

[9] Cianciolo, A., and Polsgrove, T., "Human Mars Entry, Descent and Landing ArchitectureStudy: Phase 2 Summary," *2018 AIAA SPACE and Astronautics Forum and Exposition,* Orlando, FL, 2018. https://doi.org/10.2514/6.2018-5190.

[10] Lugo, R., Dwyer-Cianciolo, A., Dutta, S., Williams, R., Pensado, A., and Chen, P.-T., "Integrated Precision Landing Performance Results for a Human-Scale Mars Landing System," *AIAA SciTech 2022 Forum,* San Diego, CA, 2022. https://doi.org/10.2514/6.2022-0607.

[11] Del Corso, J., Cheatwood, F., Bruce III, W., Hughes, S., and Calomino, A., "Advanced High-Temperature Flexible TPS for Inflatable Aerodynamic Decelerators," AIAA 2011-2510, *AIAA Aerodynamic Decelerator Systems Conference,* Dublin, Ireland, 2011.

[12] Del Corso, J., Bruce III, W., Hughes, S., Dec, J., Rezin, M., Meador, M., Guo, H., Fletcher, D., Calomino, A., and Cheatwood, F., "Flexible Thermal Protection System Development for Hypersonic Inflatable Aerodynamics Decelerators," *International Planetary Probe Workshop,* Toulouse, France, 2012.

[13] Swanson, G., Kazemba, C., Hughes, S., Williams, J., Johnson, K., Lindell, M., Bodkin, R., DiNonno, J., and Cheatwood, F., "Low-Earth Orbit Flight test of an Inflatable Decelerator (LOFTID) Aeroshell Engineering Development Unit Structural Testing," *International Planetary Probe Workshop,* Oxford, United Kingdom, 2019.

[14] Dillman, R., Hughes, S., Bodkin, R., Bose, D., Del Corso, J., and Cheatwood, F., "Flight Performance of the Inflatable Reentry Vehicle Experiment II," *International Planetary Probe Workshop,* Barcelona, Spain, 2010.

[15] Bose, D., Toniolo, M., , Cheatwood, F., Hughes, S., and Dillman, R., "Impact of Vehicle Flexibility on IRVE-II Flight Dynamics," AIAA 2011-2571*, AIAA Aerodynamic Decelerator Systems (ADS) Conference,* Dublin, Ireland, 2011. https://doi.org/10.2514/6.2011-2571.

[16] Striepe, S., Powell, R., Desai, P., Queen, E., Way, D., Prince, J., Cianciolo, A., Davis, J., Litton, D., Maddock, R., Shidner, J., Winski, R., O'Keefe, S., Bowes, A., Aguirre, J., Garrison, C., Hoffman, J., Olds, A., Dutta, S., Zumwalt, C., White, J., Brauer, G., Marsh, S., and Engel, M., *Program To Optimize Simulated Trajectories II (POST2), Vol. II: Utilization Manual,* Version 3.0.NESC, 2015.

[17] Braun, R. D., Powell, R. W., Engelund, W. C., Gnoffo, P. A., Weilmuenster, K. J., and Mitcheltree, R. A., "Mars Pathfinder Six-Degree-of-Freedom Entry Analysis," *Journal of Spacecraft and Rockets*, Vol. 32, No. 6, 1995, pp. 993–1000. https://doi.org/10.2514/3.26720.

[18] Desai, P. N., Schoenenberger, M., and Cheatwood, F. M., "Mars Exploration Rover Six-Degree-of-Freedom Entry Trajectory Analysis," *Journal of Spacecraft and Rockets*, Vol. 43, No. 5, 2006, pp. 1019–1025. https://doi.org/10.2514/1.6008.

[19] Desai, P. N., Prince, J. L., Queen, E. M., Schoenenberger, M., Cruz, J. R., and Grover, M. R., "Entry, Descent, and Landing Performance of the Mars Phoenix Lander," *Journal of Spacecraft and Rockets*, Vol. 48, No. 5, 2011, pp. 798–808. https://doi.org/10.2514/1.48239.

[20] Way, D., Davis, J., and Shidner, J., "Assessment of the Mars Science Laboratory Entry, Descent, and Landing Simulation," AAS 13-420*, AAS/AIAA Space Flight Mechanics Conference,* Kauai, HI, 2013.

[21] Maddock, R., Cianciolo, A., Korzun, A., Litton, D., Zumwalt, C., and Karlgaard, C., "InSight Entry, Descent, and Landing Postflight Performance Assessment," *Journal of Spacecraft and Rockets*, Vol. 58, No. 5, 2021, pp. 1530–1537. https://doi.org/10.2514/1.A35023.

[22] Dutta, S., Way, D. W., Zumwalt, C. H., and Blette, D. J., "Postflight Assessment of Mars 2020 Entry, Descent, and Landing Simulation," *Journal of Spacecraft and Rockets*, Vol. 61, No. 3, 2024, pp. 847–857. https://doi.org/10.2514/1.A35771.

[23] Desai, P., Lyons, D., Tooley, J., and Kangas, J., "Entry, Descent, and Landing Operations Analysis for the Stardust Entry Capsule," *Journal of Spacecraft and Rockets*, Vol. 45, No. 6, 2008, pp. 1262–1268. https://doi.org/10.2514/2.2824, URL http://doi.aiaa.org/10.2514/2.2824.

[24] Desai, P. N., Qualls, G. D., and Schoenenberger, M., "Reconstruction of the Genesis Entry," *Journal of Spacecraft and Rockets*, Vol. 45, No. 1, 2008, pp. 33–38. https://doi.org/10.2514/1.30042.

[25] Dutta, S., Karlgaard, C., Tynis, J., O'Farrell, C., Sonneveldt, B., Queen, E., Bowes, A., Leyleck, E., and Ivanov, M., "Advanced Supersonic Parachute Inflation Research Experiment Preflight Trajectory Modeling and Postflight Reconstruction," *Journal of Spacecraft and Rockets*, Vol. 57, No. 6, 2020, pp. 1387–1407. https://doi.org/10.2514/1.A34706.

[26] Dutta, S., Karlgaard, C., Korzun, A., Green, J., Tynis, J., Williams, J., Yount, B., Cassell, A., and Wercinski, P., "Adaptable Deployable Entry and Placement Technology Sounding Rocket One Modeling and Reconstruction," *Journal of Spacecraft and Rockets*, Vol. 59, No. 1, 2022, pp. 236–259. https://doi.org/10.2514/1.A35090.

[27] Francis, S., Johnson, M., Queen, E., and Williams, R., "Entry, Descent, and Landing Analysis for the OSIRIS-REx Sample Return Capsule," AAS 24-188*, AAS GNC Conference,* Breckenridge, CO, 2024.

[28] Blakeley, H. S., Bodkin, R., and Emmett, A., "Heritage to Flight; The Test Program that Brought an Inflation System Back to Life for the Low Earth Orbit Flight Test of an Inflatable Decelerator (LOFTID)," AIAA 2024-1312*, AIAA SciTech 2024,* Orlando, FL, 2024. https://doi.org/10.2514/6.2024-1312.

[29] Mendeck, G., and Carman, G., "Design for Mars Smart Landers Using the Entry Terminal Point Controller," AAS 2002-4502*, AIAA Atmospheric Flight Mechanics Conference, Monterrey, CA*, 2002.

[30] Mendeck, G., and McGrew, L., "Entry Guidance Design and Postflight Performance for 2011 Mars Science Laboratory Mission," *Journal of Spacecraft and Rockets*, Vol. 51, No. 4, 2014, pp. 1094–1105. https://doi.org/10.2514/1.A32737.

[31] Chen, A., et al., "Mars 2020 Entry, Descent, and Landing As-Flown Report," Tech. rep., Jet Propulsion Laboratory, IOM-M2020-630-22-001, 2022.

[32] Lu, P., "Entry Guidance: A Unified Method," *Journal of Guidance, Control, and Dynamics*, Vol. 37, No. 3, 2014, pp. 713–728. https://doi.org/10.2514/1.62605.

[33] Korzun, A., Hollis, B. J., Wise, A. J., Liechty, D. S., Karlgaard, C. D., and Deshmukh, R. G., "Aerodynamic Performance of the Low-Earth Orbit Flight Test ofan Inflatable Decelerator (LOFTID) Technology DemonstrationMission," AIAA 2024-1500*, AIAA SciTech 2024,* Orlando, FL, 2024. https://doi.org/10.2514/6.2024-1500.

[34] Wright, H., Cutright, A., Corliss, J., Bruce, W., Trombetta, D., Mazaheri, A. R., Coleman, M., Olds, A., and Hancock, S., "HEART Flight Test Overview," *9th International Planetary Probe Workshop,* Toulouse, FR, 2012.

[35] Gillette, J. E., Larson, C., and Reed, J. G., "Vulcan Centaur Reuse: The Next Step toAccessible and Affordable Space," AIAA 2022-4253*, AIAA ASCENT 2022 Forum,* Las Vegas, NV, 2022. https://doi.org/10.2514/6.2022-4253.

[36] Hollis, B. R., Wise, A. J., Liechty, D. S., Korzun, A. M., Thompson, K. B., Rodrigues, N. S., and Rieken, E. F., "Aerothermodynamic Analyses for the LOFTID TechnologyDemonstration Mission," AIAA-2024-1498, *AIAA SciTech 2024 Forum,* Orlando, Florida, 2024.

[37] Sutton, K., and Randolph A. Graves, J., "A General Stagnation-point Convective-heating Equation for Arbitary Gas Mixtures," Tech. rep., NASA TR R-376, 1971.

[38] Leslie, F., and Justus, C., "The NASA Marshall Space Flight Center Earth Global Reference Atmosphere Model - 2010 Version," Tech. rep., NASA/TM-2011-216467, 2011.

[39] White, P., and Hoffman, J., "Earth Global Reference Atmospheric Model (Earth-GRAM): User Guide," Tech. rep., NASA TM 2021-0022157, 2021.

[40] Graves, C. A., and Harpold, J. C., "Apollo Experience Report - Mission Planning for Apollo Entry," Tech. rep., NASA TN D-6725, 1972.

[41] Hall, J., Noca, M., and Bailey, R., "Cost-Benefit Analysis of the Aerocapture Mission Set," *Journal of Spacecraft and Rockets*, Vol. 42, No. 2, 2005, pp. 309–320. https://doi.org/10.2514/1.4118.

[42] Mann, S. C., Bowes, A., Deshmukh, R., and Dutta, S., "Small Satellite-sized Hypersonic Inflatable Aerodynamic Decelerators for Interplanetary Science Missions," SSC22-WKIV-07*, Small Satellite Conference,* Logan, UT, 2022. URL https://digitalcommons.usu.edu/cgi/viewcontent.cgi?article=5222&context=smallsat.

[43] Tobin, S. A., Brune, A. J., and Bowes, A. L., "Probabilistic Aeroshell Thermal Response Uncertainty Analysis for the LOFTID Technology Demonstration Mission," AIAA-2024-1499, *AIAA SciTech 2024 Forum,* Orlando, Florida, 2024. https://doi.org/10.2514/6.2024-1499.

[44] Desai, P. N., Blanchard, R. C., and Powell, R. W., "Entry trajectory and atmosphere reconstruction methodologies for the Mars Exploration Rover mission," *International Planetary Probe Workshop*, 2004.

[45] Desai, P., "Mars Exploration Rovers Entry, Descent, and Landing Trajectory Analysis," 2004-5092, *AIAA/AAS Astrodynamics Specialist Conference,* Providence, RI, 2004. URL http://grctechlib.grc.nasa.gov/public/digital/sg/MarsScout/MarsExplorationRoversEntry,Descent,andLandingTrajectoryAnalysis.pdf.